Petrogenesis and mantle source characteristics of Triassic alkaline basaltic rocks of North Kamarbon, Northern Central Alborz, Iran

Roghieh Doroozi [a,*], Carmela Vaccaro [b], Fariborz Masoudi [a], Riccardo Petrini [c]

[a] Faculty of Earth Science, Shahid Beheshti University, Velenjak, Tehran, Iran
[b] Department of Mineralogy, University of Ferrara, C.so E. 1º d'Este 32, 44100 Ferrara, Italy
[c] Department of Earth Sciences, University of Pisa, Via S. Maria 53, 56126 Pisa, Italy

Abstract

The Triassic alkaline basaltic rocks (TABR) of North Kamarbon are located in Central Alborz, which is regarded as the northern part of the Alpine-Himalayan orogenic belt. Fractional crystallization does not appear as a major process in the genesis of TABR while different degree of partial melting may be regarded as the main process, based on petrography and geochemistry studies. The geochemical characteristics of TABR are in conflict with a substantial involvement of continental crust or crustal contamination. High $(La/Yb)_N$ and $(Dy/Yb)_N$ ratios, along with other geochemical features, in the TABR magma, suggest an asthenospheric origin, with low degree of partial melting of a garnet-bearing mantle sources. Enrichment patterns of LILE (Ba, Sr and Th), HFSE (Nb, Ta and Zr) and P, and depletion at HREE (Yb, Lu) are similar to what observed for OIB or intraplate alkaline magmatic rocks. The Sr and Nd isotopic ratios range from 0.70448 to 0.70522 and from 0.51269 to 0.51280, respectively, suggesting time-integrated slightly depleted magma sources. The data indicate that the evolution of TABR could be related to the rifting basin, in Late Triassic, which caused their development by upwelling and decompressional melting of an asthenospheric mantle, without a major involvement of subcontinental lithospheric mantle or crustal contamination.

1. Introduction

The Central Alborz, which is a part of the Alpine-Himalayan orogenic belt, includes the different volcanism phases with the wide range of magmatic rocks in this area during Mesozoic (Assereto, 1966; Stampfli, 1978; Berberian, 1983; Alavi, 1996; Nazari et al., 2004; Shahidi, 2005). In the Central Alborz, Mesozoic alkaline magmatic rocks are attributed to the Triassic, Jurassic and Cretaceous (Cartier, 1971; Saidi and Ghassemi, 1993; Vahdati Daneshmand and Nadim, 1999). The Triassic alkaline basaltic rocks (TABR) in the Kamarbon area in the northern part of Central Alborz,

overly Carnian massive dolomites and are beneath Norian-Rhaetian sandstones, supporting the Late Triassic age (Saidi and Ghassemi, 1993), even if there are no corresponding radiometric ages available (Fig. 1). The alkaline volcanic phase, in the study area, could be an indicator for the intra-continental tectonic setting linked to a rift system in Central Alborz during Late Triassic (Steiger, 1966; Nabavi and Seyed Emami, 1977; Berberian and King, 1981; Berberian, 1983; Annels et al., 1985; Fauvelet and Eftekhar Nezhad, 1992; Sabzehei, 1993; Seyed Emami, 2003; Brunet et al., 2003; Shahidi, 2005; Shahidi, 2008; Nazari and Shahidi, 2011).

In the Kamarbon area, the outcrop of TABR allows us to investigate the Triassic alkaline volcanism of the Alpine Himalayan orogenic belt in Iran. In particular, geochemical and petrological studies on alkaline volcanic rocks may lead to explain the different contribution of the processes like

---

* Corresponding author. Fax: +982165573318.
Peer review under responsibility of Guangzhou Institute of Geochemistry.
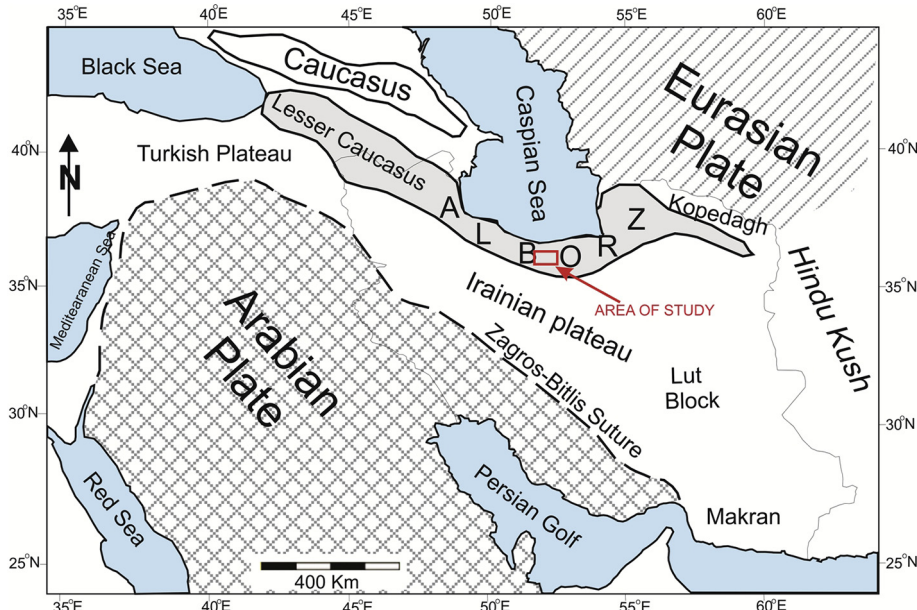   *E-mail address:* r.doroozi220@gmail.com (R. Doroozi).

Fig. 1. General tectonic map of Iran with Arabian and Eurasian plate and the location of studied area in Central Alborz zone.

fractional crystallization, magma mixing or crustal contamination in magma genesis (Hawkesworth and Vollmer, 1979; McKenzie and Bickle, 1988; Wilson, 1989; Rollinson, 1993; Hallman, 1996; Best, 2002; McBirney, 2006).

Little is known about the Paleozoic and Mesozoic igneous activities in Central Alborz, whereas only few aspects are known for the Cenozoic magmatic activity. However, neither whole-rock geochemistry nor microprobe or isotopic data have been so far published for the TABR of the Kamarbon area. In this study, major and trace elements, mineral electron microprobe data and Sr–Nd isotopic analysis of TABR are used to provide constrains on the composition of mantle sources, depth and degree of partial melting related with this magmatism. The results of this study may contribute to elucidate the genesis of the Triassic magmatism that produced the alkaline volcanic rocks in Alpine Himalayan orogenic belt in Central Alborz.

2. Geological background and the occurrence of the TABR

Central Alborz was a part of Gondwana in the early Paleozoic. It separated from Gondwana during Ordovician to Silurian and then collided with Eurasian plate in the Triassic, causing the Paleotethys Ocean closure to the north, and the formation of the Neotethys Ocean to the south (Stocklin, 1974; Berberian and King, 1981; Stampfli et al., 1991). After the Triassic collisional event, along both sides of the Neotethys Ocean intracontinental compressions were initiated and accompanied by deposition of the coal bearing Shemshak Formation (Berberian, 1983). After the compressional movements and uplift, the Mesozoic extensional phases started, marked by the Rhaetic rift volcanism. The early Jurassic extensional phases and subsidence which were also recorded in the West of Alborz (Caucasus) resulted by the formation of

the oceanic basin along the Sevan-Akera suture zone (Adamia et al., 1977; Berberian et al., 1982).

In the Central Alborz, the Early Triassic carbonates are overlapped by the Late Triassic shales and sandstones. Extensional phases in the area started in the Late Triassic associated with alkaline igneous activity (Berberian and King, 1981; Berberian, 1983). The occurrence of alkaline lavas and pyroclastic rocks interbedded with the Late Triassic shales and sandstones reveals the existence of an extensional system in Central Alborz (Nazari et al., 2004). The evolution of this extensional regime can generate the basins of Caspian Sea and Black Sea in Late-Middle Jurassic (Nazari, 2006).

During Late Triassic, the structural features of the lower part of Shemshak Formation reveal an important extensional system with several occurrences of normal faults. This extensional regime is also registered in the lower part of the Shemshak Formation by changes in thickness. These changes are related to the activity of big normal faults or thrust faults in Central Alborz (Nazari and Shahidi, 2011).

Allenbach (1966) claimed that the outcrops of several alkaline dykes inside the Shemshak Formation prove the occurrence of extensional phases and continental fracturing during the Middle Triassic-Late Jurassic in Central Alborz. TABR have been placed on the Carnian massive dolomites of Elika Formation, covered by Norian-Rhaetian sandstones and clays of late Triassic (Saidi and Ghassemi, 1993) (Fig. 2).

Fig. 3 and Fig. 4a illustrate that the TABR locate above the Carnian Elika massive dolomites and beneath the Late Triassic Shemshak sandstones, indicating Late Triassic age of the magmatism. Exfoliation and mechanical weathering are observed in some of TABR samples (Fig. 4b). Also in Central Alborz, there are several small gabbroic intrusions that are emplaced inside the Shemshak Formation (Saidi and Ghassemi, 1993).

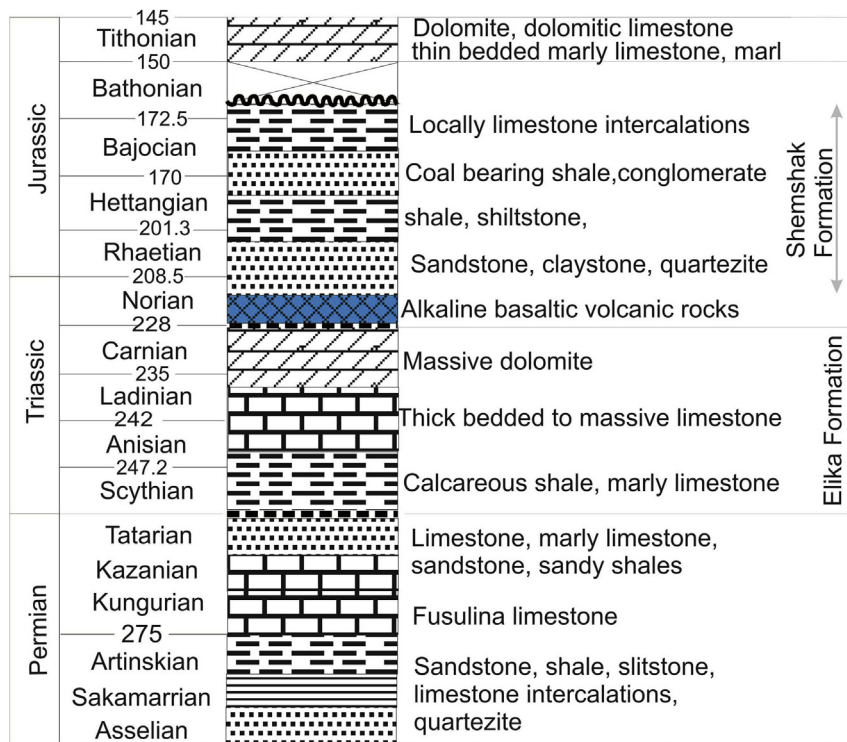Fig. 2. Geological map of the study area. Modified from the geological map of 1/100000 Marzanabad, Iran.

Fig. 3. Stratigraphic column of the Triassic and Jurassic rocks within the Kamarbon area, after Vahdati Daneshmand and Nadim (1999).

TABR are dark gray to dark green in hand specimen (Fig. 4b). The rocks are mainly analcime olivine basalts with mostly porphyritic texture. Phenocrysts of TABR are pyroxene, olivine and rare plagioclase. The most abundant mineral in TABR is euhedral to subhedral pyroxene that can observe with the grain size up to 2 cm (Fig. 5a, b and c). They mostly reveal plane polarized pink color which can be the sign of high amount of Ti (Jung, 2003). Some of the pyroxenes show the glomeroporphyric texture (Fig. 4d). Olivine is the second mineral in terms of abundance, showing wide alteration to chlorite and some iddingsite (Fig. 5a and c). The rare plagioclase phenocrysts mostly show alterations to sericite, albite and calcite. Groundmass of TABR contains pyroxene, olivine, plagioclase, analcime and accessory minerals as opaque and apatite. The groundmass olivines as the phenocryst olivines exhibit alteration to iddingsite and chlorite. The alteration to iddingsite in groundmass olivines is more common, possibly indicating the more fayalitic composition. Anhedral analcime in groundmass crystallized between pyroxene and olivine, indicating it is a late-stage crystallized phase (Fig. 5e and f).
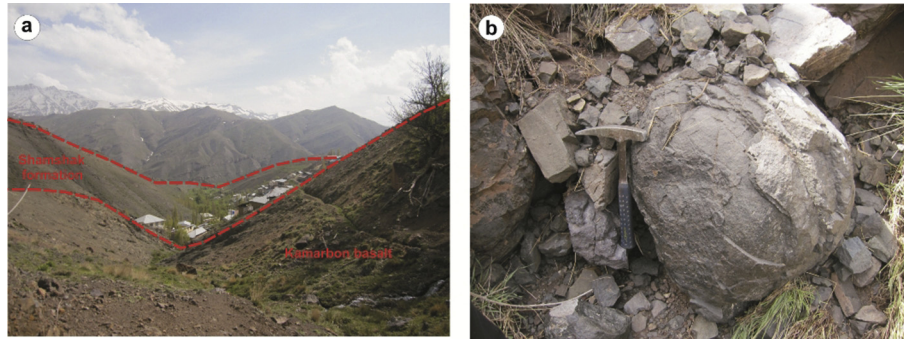
Fig. 4. Field photographs showing (a) TABR in contact with the late Triassic sandstones (b) Exfoliation mechanical weathering in TABR.
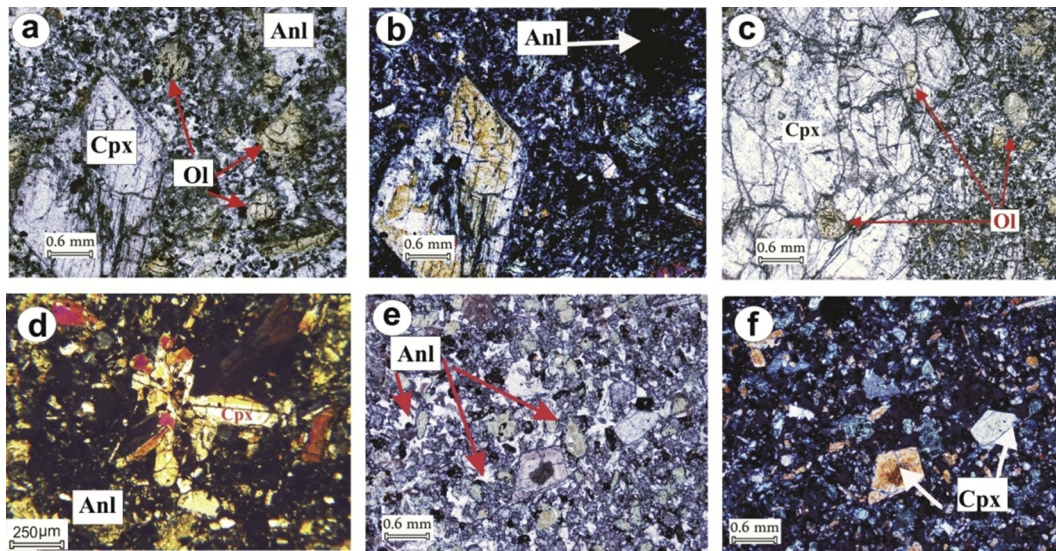

Fig. 5. Clinopyroxene (Cpx), analcime (Anl) and olivine (Ol) minerals in TABR (a, c and e) Plane polarized light image (b, d and f) Cross-polarized transmitted light images.

3. Analytical methods

Samples with the most possible unaltered chips were selected and powdered in an agate mill. X ray fluorescence (XRF) analyses for major and some trace elements (Ni, Co, Cr, V, Sr, Ba and Rb) were performed on powder pellets, using a wavelength-dispersive automated Philips PW 1400 spectrometer at the Department of Earth Sciences of Ferrara University in Italy, based on the method by Franzini et al. (1975) and Leoni and Saitta (1976) for matrix correction. Accuracy and precision for major elements are estimated as better than 3% for Si, Ti, Fe, Ca and K, and 7% for Mg, Al, Mn, Na; for trace elements (above 10 ppm) they are better than 10%. Trace and rare-earth elements were analyzed by inductively coupled plasma mass spectrometry (ICP-MS) at the same place, using a VG Plasma Quad2 plus. Accuracy and precision, based on replicated analyses of samples and standards, are estimated as better than 10% for all elements well above the detection limit.

Mineral compositions were measured at the Department of Mineralogy of Padua University in Italy, with a Cameca–Camebax electron microprobe (fitted with three spectrometers) at accelerating voltage of 15 kV, and beam current of 15 nA, using natural silicates and oxides as standards. The beam was enlarged to a diameter of 5 μm and the counting times were set to 10 s for both peak and background and the data correction was performed using PAP methods (Pouchou and Pichoir, 1984).

Isotopic analyses on whole rocks were carried out at the Department of Mathematics and Geosciences of Trieste University in Italy; whole-rock was leached with hot 6N HCl and then totally digested with HF–HNO$_3$. Strontium and REE were separated by using standard cation exchange chromatographic columns with an AG 50W - X8 resin using 2.5N HCl for Sr and 6N HCl for the REE as an eluent. Nd was separated from the other REE by reversed-phase chromatography using HDEHP-coated Teflon columns and 0.12N HCl. The isotopic compositions were measured by using a VG Micromass 54E mass spectrometer for both Sr and Nd isotopes. Repeated analysis of the NIST − NBS 987 reference standard gave an average of $^{87}Sr/^{87}Sr = 0.71024 \pm 0.00004$ (2SD) (n = 45) and no correction was applied for instrumental bias. The total procedural blank for Sr was less than 50 pg. Repeated measurements of the JNd-i standard (in consistency with La Jolla

standard) yielded an average of 143Nd/144Nd of 0.512118 ± 0.000018 (2SD) (n = 45) in agreement within experimental errors with the certified value of 0.5121116. The total procedural blank for Nd was less than 30 pg. The measured Sr and Nd isotope-ratios were back-calculated to Upper Triassic by using the radioactive decay equation and the proper decay constants (Dickin, 2005). The Sr and Nd isotope ratios were corrected by normalizing to the average $^{87}Sr/^{86}Sr$ ratio for the standard NIST NBS-987 = 0.710244 ± 0.000036 and the average $^{143}Nd^{/144}Nd$ ratio for the standard JNDi = 0.51200 ± 0.000008.

3.1. Mineral chemistry

Representative compositions of pyroxenes are shown in Table 1. Pyroxene is the main mineral in TABR. In the pyroxene classification diagram of Morimoto et al. (1988) all analyzed samples reveal diopside composition, although some of them show tendency toward more calcic pyroxene (Fig. 6). Pyroxenes of feldespatoid bearing alkaline rocks or teschenites can be plotted above diopside field because of their high contents of Al and Ti that cause the analyzed points to be above the diopside field (Wlodyka, 2002; Bardintzeff et al., 2012). The chemical composition of pyroxenes in TABR ranges from $Wo_{44.3}$ $Fs_{9.3}$ $En_{46.4}$ at core to $Wo_{50.6}$ $Fs_{13.9}$ $En_{35.4}$ at rim that shows enrichment of Fe and Ca and depletion of Mg at rims. The composition of fine pyroxenes in groundmass reveals higher values of FeO than phenocrysts rims.

Representative compositions of feldspars are shown in Table 2. Only the plagioclases in groundmass are analyzed due to the striking alteration of the rare plagioclase phenocrysts. Compositions of the plagioclases in the groundmass of TABR plot in the field of labradorite, ranging from $Ab_{31.0}An_{65.3}Or_{3.6}$ to $Ab_{41.6}An_{55.0}Or_{3.2}$ (Fig. 7). Most of the plagioclases have undergone weathering and display alteration to secondary minerals like sericite, clay, albite and zeolite.

Representative compositions of analcimes are shown in Table 3. The analcimes of TABR are colorless in thin section and isotropic. This mineral crystallized interstitially among olivine, pyroxene and plagioclase minerals. Analcimes have Na_2O 9.35−10.53 wt.%; Fe_2O_3 (0.01−0.06 wt.%); K_2O, 0.02−0.16 wt. %; [Na/(Na + K)], 0.99 and the high values of Na_2O/K_2O ratio (ranging from 3.58 to 7.48). Analcime regarded as a widespread mineral occurring in many different kinds of environments and can occur in igneous rocks as primary or secondary mineral (Deer et al., 2004). The analcimes of TABR are regarded as secondary analcimes that can produced by alteration of other minerals during the crystallization process.

3.2. Major elements, trace elements and isotope geochemistry

All samples in this study are plotted in the field of alkali-basalt in the Winchester and Floyd classification diagram (1977) (Fig. 8). SiO2, MgO and Mg# [Mg-number = 100(Mg/ Mg + Fe$_{total}$)] range from 42.24 to 45.21 wt.%, 10.95 to 15.49 wt.% and 60.28 to 69.81, respectively (Table 4). There is no any systematic observed pattern between the variations of major oxides (SiO_2, Al_2O_3, Na_2O, K_2O, Fe_2O_3 and CaO) versus MgO in TABR. The studied rocks show a range of trace element contents that Ni, Co and Cr vary from 222 to 289 ppm, from 59 to 72 ppm and from 251 to 358 ppm respectively.

All the TABR samples are enriched in high field strength elements (HFSE) like Y (20−30 ppm), Zr (165−200 ppm) and Nb (63−73 ppm) with respect to primitive mantle. They are also enriched in LREE with respect to HREE in chondrite-normalized diagrams (Fig. 9a), with $(La/Yb)_N$ and $(Dy/Yb)_N$ ratios ranging from 17.42 to 20.05 and 1.52 to 1.62, respectively.

Sm−Nd and Rb−Sr Isotopic analyses of TABR are reported in Table 5 and Table 6. The measured Sr and Nd isotope-ratios were back-calculated to Upper Triassic by using the radioactive decay equation and the proper decay constants (Dickin, 2005). The studied samples locate close in the slightly depleted part relative to bulk Earth composition regard to their $^{87}Sr/^{86}Sr$ (0.70448−0.70522) and high $^{143}Nd/^{144}Nd$ (0.51269−0.51280) (Fig. 10). They typically lie in the isotopic composition of OIB field.

4. Discussion

4.1. Alteration effects on the mobility of elements

Petrographic evidence and the relatively high LOI (ranging from 1.00 wt.% to 3.2 wt.%, Table 4) indicate that TABR have been altered to various extent. For instance the analcime mineral in TABR was produced by the alteration of primary nepheline as a result of the increment of H_2O during the crystallization process. If analcime was a primary phase and generated during fractional crystallization, it typically would contain $Fe_2O_3 \geq 1$ wt.% (Luhr and Kyser, 1989). However, the Fe_2O_3 in analcime of TABR is between 0.01 and 0.06 wt.%, likely indicating their secondary origin. Secondary analcime can be formed by the reaction of leucite + Na + $H_2O \leftrightarrow$ Analcime + K in volcanic rocks (Gupta and Fyfe, 1975; Taylor and Mackenzie, 1975). These secondary analcime contain $Fe_2O_3 \approx 0.3$ wt.% and $K_2O \geq 1$ wt.% (Luhr and Kyser, 1989). It should be considered that the presence of primary leucite in alkaline rocks is usually accompanied by the presence of other K-enriched minerals (like alkali feldspar), while in TABR there is the lack of alkali feldspar and other K-enriched phases. The amount of Fe_2O_3 (0.01−0.06 wt.%) and K_2O (0.02−0.16 wt. %) in analcime of TABR, coupled with the high values of Na_2O/K_2O ratio (ranging from 3.58 to 7.48) and the lack of potassic mineral phases in TABR samples demonstrate that the analcime is an alteration product (Morata et al., 2005; Morata and Higueras, 1996).

The occurrence of alteration is reflected by the variability in concentration of the most mobile elements (e.g. K_2O, Na_2O, Rb and Ba, Table 4) although transition metals (e.g. Cr and Ni), high-field strength elements (e.g. Ti, Zr, Y, Nb and REE) remain relatively immobile under low-temperature alterations

Table 1
Representative microprobe analysis of pyroxenes in TABR, values are given in wt.%. The structural formula calculation is based on six oxygens and cations are in apfu (atoms per formula unit).

Sample	RD122	RD122	RD122	RD122	RD122	RD182	RD182	RD182	RD182	RD182	RD182	RD182	RD122	RD122	RD122
Note	core	rim	core	middle	rim	core	middle	rim	core	rim	rim	rim	rim	core	middle
SiO_2	49.46	43.90	46.47	47.88	47.69	47.50	43.84	47.38	48.44	47.28	47.39	47.11	43.42	47.73	52.33
TiO_2	1.30	2.93	1.88	1.73	1.80	1.90	3.17	2.23	1.82	2.30	2.24	2.22	3.67	2.27	0.71
Al_2O_3	5.02	8.52	7.58	5.14	7.18	7.46	9.12	5.76	4.93	5.88	6.26	5.65	9.40	5.55	4.89
Cr_2O_3	0.42	0.03	0.63	0.16	0.05	0.66	0.00	0.01	0.21	0.03	0.00	0.03	0.08	0.00	0.13
FeO	5.69	7.47	5.82	6.41	7.62	5.79	7.87	7.14	6.75	7.17	6.94	7.14	7.87	7.23	5.95
MnO	0.10	0.13	0.10	0.11	0.22	0.11	0.07	0.10	0.13	0.17	0.10	0.07	0.17	0.14	0.15
MgO	14.80	11.80	13.15	14.27	12.98	13.34	11.68	13.71	13.96	13.48	13.32	13.61	11.48	13.47	13.37
CaO	21.80	22.60	21.99	22.09	21.01	22.22	22.72	22.98	22.87	23.07	22.97	23.09	22.81	22.69	22.37
Na_2O	0.52	0.49	0.60	0.40	0.71	0.63	0.50	0.42	0.36	0.38	0.43	0.41	0.52	0.41	0.96
Total	99.10	97.86	98.24	98.20	99.25	99.60	98.98	99.74	99.47	99.76	99.65	99.33	99.42	99.50	100.87
Si	1.83	1.67	1.74	1.80	1.78	1.76	1.65	1.76	1.80	1.76	1.76	1.76	1.63	1.78	1.91
Ti	0.04	0.08	0.05	0.05	0.05	0.05	0.09	0.06	0.05	0.06	0.06	0.06	0.10	0.06	0.02
Al	0.22	0.38	0.34	0.23	0.32	0.33	0.40	0.25	0.22	0.26	0.27	0.25	0.42	0.24	0.21
Cr	0.01	0.00	0.02	0.00	0.00	0.02	0.00	0.00	0.01	0.00	0.00	0.00	0.00	0.00	0.00
Fe^{3+}	0.07	0.15	0.10	0.10	0.08	0.08	0.16	0.14	0.10	0.13	0.11	0.14	0.15	0.10	0.00
Fe^{2+}	0.11	0.09	0.09	0.10	0.16	0.10	0.09	0.08	0.11	0.10	0.11	0.08	0.09	0.12	0.18
Mn	0.00	0.00	0.00	0.00	0.01	0.00	0.00	0.00	0.00	0.01	0.00	0.00	0.01	0.00	0.00
Mg	0.82	0.67	0.74	0.80	0.72	0.74	0.66	0.76	0.77	0.75	0.74	0.76	0.64	0.75	0.73
Ca	0.87	0.92	0.88	0.89	0.84	0.88	0.92	0.91	0.91	0.92	0.91	0.92	0.92	0.91	0.87
Na	0.04	0.04	0.04	0.03	0.05	0.04	0.04	0.03	0.03	0.03	0.03	0.03	0.04	0.03	0.07
Total	4.00	4.00	4.00	4.00	4.00	4.00	4.00	4.00	4.00	4.00	4.00	4.00	4.00	4.00	4.00
Al ^{IV}	0.17	0.33	0.26	0.20	0.22	0.24	0.35	0.24	0.20	0.24	0.24	0.24	0.37	0.22	0.09
Al ^{VI}	0.05	0.05	0.08	0.03	0.09	0.08	0.05	0.01	0.02	0.01	0.04	0.00	0.04	0.02	0.12
Wo	46.46	50.29	48.97	46.97	46.49	48.96	50.30	48.17	47.99	48.51	48.87	48.45	50.62	48.09	48.91
En	43.91	36.53	40.73	42.21	39.97	40.90	35.99	39.99	40.74	39.44	39.43	39.74	35.44	39.72	40.68
Fs	9.64	13.19	10.30	10.81	13.54	10.14	13.71	11.85	11.27	12.05	11.70	11.81	13.93	12.19	10.41
Mg#	88.36	88.45	89.53	89.13	81.97	87.96	87.66	89.98	87.35	88.66	87.34	90.67	87.31	85.83	80.03
Ti/Al	0.16	0.22	0.16	0.22	0.16	0.16	0.22	0.25	0.24	0.25	0.23	0.25	0.25	0.26	0.09

| Sample	RD122	RD122	RD121a	RD121a	RD121a	RD121a	RD121a	RD121a	RD35	RD35	RD35	RD35	RD35	RD35	RD35
Note	rim	rim	core	middle	rim	core	core	rim	rim	core	rim	core	rim	groundmass	groundmass
SiO_2	49.69	48.61	46.73	42.67	44.16	49.49	50.71	46.24	44.56	42.39	44.57	46.50	44.12	43.19	45.40
TiO_2	1.06	1.49	2.42	3.83	2.99	0.92	0.92	2.62	3.05	4.16	3.28	2.52	3.33	3.23	3.05
Al_2O_3	5.36	6.20	6.06	9.61	8.62	4.84	4.81	6.77	8.93	10.38	8.37	6.14	8.74	8.65	11.37
Cr_2O_3	0.11	0.10	0.00	0.02	0.05	1.21	0.76	0.07	0.03	0.02	0.20	0.00	0.21	0.09	0.00
FeO	5.71	5.80	7.45	7.85	7.56	5.18	5.47	7.20	7.66	8.11	7.32	7.25	7.45	8.05	8.34
MnO	0.10	0.09	0.18	0.10	0.13	0.15	0.11	0.14	0.11	0.14	0.09	0.12	0.13	0.12	0.13
MgO	13.43	13.44	13.22	11.28	12.05	15.00	15.68	12.92	11.89	11.02	12.01	13.11	11.71	11.42	11.10
CaO	22.90	23.18	23.08	22.96	23.00	20.86	20.80	23.11	22.84	23.20	23.04	23.27	23.12	23.07	18.12
Na_2O	0.83	0.88	0.45	0.50	0.44	0.57	0.62	0.43	0.51	0.41	0.43	0.40	0.45	0.51	1.45
Total	99.18	99.77	99.58	98.83	99.02	98.22	99.88	99.49	99.60	99.84	99.33	99.31	99.25	98.33	99.81
Si	1.84	1.79	1.74	1.61	1.66	1.85	1.86	1.72	1.66	1.59	1.67	1.74	1.66	1.64	1.69
Ti	0.03	0.04	0.07	0.11	0.08	0.03	0.03	0.07	0.09	0.06	0.09	0.04	0.09	0.09	0.09
Al	0.23	0.27	0.27	0.43	0.38	0.21	0.21	0.30	0.39	0.46	0.37	0.27	0.39	0.39	0.50
Cr	0.00	0.00	0.00	0.00	0.00	0.04	0.02	0.00	0.00	0.00	0.01	0.00	0.01	0.00	0.00
Fe^{3+}	0.08	0.13	0.15	0.17	0.16	0.04	0.05	0.13	0.14	0.16	0.13	0.14	0.14	0.19	0.06
Fe^{2+}	0.10	0.05	0.08	0.08	0.07	0.12	0.12	0.09	0.10	0.09	0.10	0.09	0.10	0.07	0.20
Mn	0.00	0.00	0.01	0.00	0.00	0.00	0.00	0.00	0.00	0.00	0.00	0.00	0.00	0.00	0.00
Mg	0.74	0.74	0.73	0.63	0.67	0.84	0.86	0.72	0.66	0.62	0.67	0.73	0.66	0.65	0.62
Ca	0.91	0.91	0.92	0.93	0.93	0.83	0.82	0.92	0.91	0.93	0.93	0.93	0.93	0.94	0.72
Na	0.06	0.06	0.03	0.04	0.03	0.04	0.04	0.03	0.04	0.03	0.03	0.03	0.03	0.04	0.10
Total	4.00	4.00	4.00	4.00	4.00	4.00	4.00	4.00	4.00	4.00	4.00	4.00	4.00	4.00	4.02
Al ^{IV}	0.16	0.21	0.26	0.39	0.34	0.15	0.14	0.28	0.34	0.41	0.33	0.26	0.34	0.36	0.31
Al ^{VI}	0.08	0.06	0.01	0.04	0.04	0.06	0.07	0.02	0.06	0.05	0.04	0.01	0.04	0.03	0.19
Wo	49.65	49.88	48.67	51.18	50.25	45.46	44.28	49.37	50.25	51.59	50.61	49.24	51.00	50.88	45.10
En	40.52	40.23	38.78	34.98	36.64	45.48	46.45	38.40	36.39	34.10	36.69	38.59	35.94	35.06	38.44
Fs	9.83	9.89	12.55	13.83	13.11	9.06	9.28	12.23	13.36	14.31	12.70	12.17	13.06	14.07	16.46
Mg#	88.43	93.58	89.82	88.91	90.15	87.71	87.73	88.92	87.32	86.78	86.92	89.57	87.22	90.37	75.23
Ti/Al	0.13	0.15	0.25	0.25	0.22	0.12	0.12	0.25	0.22	0.13	0.25	0.15	0.24	0.24	0.17
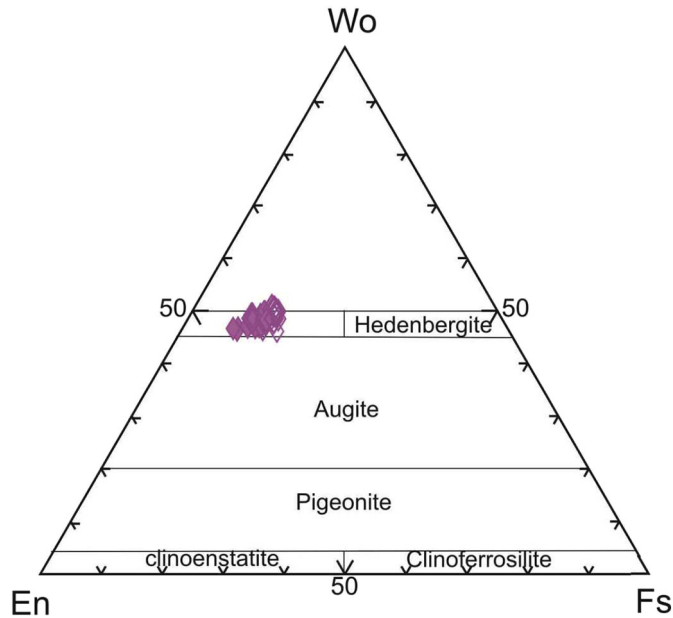
Fig. 6. Pyroxenes of TABR in the classification ternary diagram of pyroxenes (Morimoto et al., 1988). Closed symbols represent phenocryst core whereas open ones represent phenocryst rim.
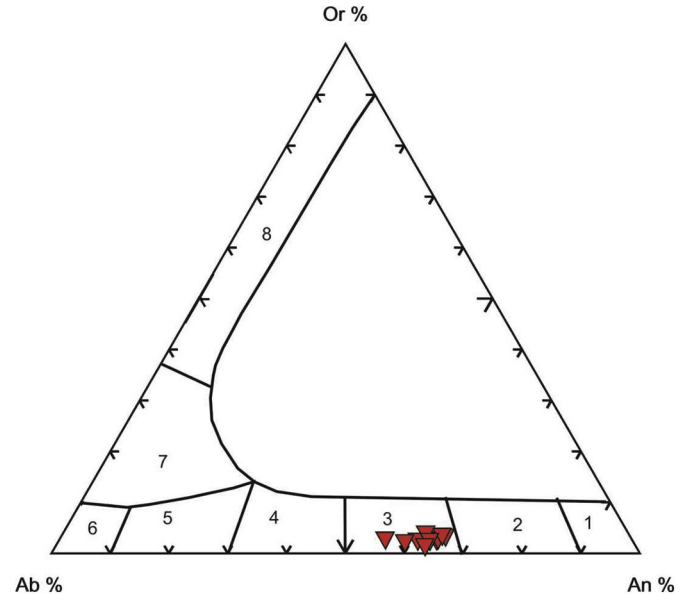

Fig. 7. Composition of plagioclases from TABR in the ternary diagram of plagioclases, 1 = Anorthite. 2 = Bytownite. 3 = Labradorite. 4 = Andesine. 5 = Oligoclase. 6 = Albite. 7 = Anorthoclase. 8 = Sanidine.

(Pearce and Cann, 1973; Winchester and Floyd, 1977; Bienvenu et al., 1990; Dai et al., 2011).

It is assumed that TABR preserve their pristine HFSE characteristics because of the uniform HFSE abundances (Table 4). Hence, HFSE$_S$ and the ratios like Zr/Ce, Zr/Nb, Th/Nb, La/Ta, La/Yb, Ce/Yb, Sm/Yb, Dy/Yb and Zr/La will be used in the following discussion in order to investigate the possible magma mantle sources.

4.2. The role of crustal contamination

Zr/Nb ratio in TABR samples varies from 2.13 to 2.81. However this ratio ranges from 2 to 4 in alkaline igneous rocks

and from 8 to 12 in the continental crust samples (Weaver, 1991) which is possibly indicating the lack of a significant crustal contamination in the studied rocks (Wörner 1999). The (Th/Nb)$_N$ vs. (La/Nb)$_N$ diagram is used to show the continental crustal contamination effects (Dai et al., 2011) (Fig. 11). In this diagram all samples place near to the field of OIB and far from the lower crust composition, supporting the hypothesis that the crustal contamination process in these rocks, if occurred, is a minor process. The lack of Ti and other HFSE negative anomalies, as well as the presence of a negative anomaly of K in primitive mantle-normalized multilemental diagrams, are incompatible with a substantial involvement of continental crust in the genesis of TABR (Fig. 9b).

Table 2
Representative microprobe analysis of plagioclases in TABR, values are given in wt.%. The structural formula calculation is based on eight oxygens and cations are in apfu (atoms per formula unit).

Sample	RD121a	RD121a	RD121a	RD122	RD122	RD122	RD182	RD182	RD182	RD182
SiO$_2$	52.17	50.81	52.91	50.98	51.98	52.17	51.17	50.91	52.98	51.55
TiO$_2$	0.18	0.14	0.17	0.21	0.16	0.21	0.18	0.16	0.19	0.16
Al$_2$O$_3$	29.75	30.93	28.67	31.10	30.98	29.97	30.75	31.02	28.76	31.01
FeO	0.57	0.52	0.52	0.67	0.58	0.61	0.65	0.56	0.55	0.66
K$_2$O	0.18	0.54	0.32	0.59	0.57	0.12	0.44	0.25	0.33	0.55
CaO	12.14	12.62	12.88	11.98	12.21	12.78	12.85	12.88	11.89	12.32
Na$_2$O	4.45	3.80	3.99	5.01	3.21	4.02	3.45	4.21	4.85	3.55
Total	99.48	99.43	99.54	100.58	99.78	99.93	99.55	100.05	99.60	99.88
Si	2.37	2.32	2.40	2.31	2.35	2.36	2.33	2.31	2.41	2.33
Ti	0.01	0.00	0.01	0.01	0.01	0.01	0.01	0.01	0.01	0.01
Al	1.59	1.66	1.54	1.66	1.65	1.60	1.65	1.66	1.54	1.65
Ca	0.59	0.62	0.63	0.58	0.59	0.62	0.63	0.63	0.58	0.60
Na	0.39	0.34	0.35	0.44	0.28	0.35	0.30	0.37	0.43	0.31
K	0.01	0.03	0.02	0.03	0.03	0.01	0.03	0.01	0.02	0.03
Total	5.01	5.02	4.99	5.08	4.96	5.00	4.94	4.99	4.98	4.93
Ab %	39.45	34.14	35.25	41.69	31.07	36.02	31.81	36.63	41.68	33.12
An %	59.52	62.65	62.88	55.09	65.31	63.26	65.52	61.93	56.46	63.51
Or %	1.02	3.21	1.87	3.22	3.61	0.73	2.67	1.43	1.87	3.38

Table 3
Representative microprobe analysis of analcimes in TABR, values are given in wt.%. The structural formula calculation is based on six oxygens and cations are in apfu (atoms per formula unit).

| Sample	RD122	RD122	RD122	RD121a	RD121a	RD121a	RD182	RD182	RD182	RD182
SiO_2	55.47	55.51	55.94	56.15	55.81	62.43	56.47	57.22	54.88	56.04
TiO_2	0.11	0.12	0.11	0.16	0.15	0.00	0.10	0.10	0.10	0.13
Al_2O_3	25.64	25.40	24.97	25.19	25.30	21.81	25.33	25.66	25.72	25.27
FeO	0.29	0.14	0.21	0.21	0.17	0.59	0.32	0.18	0.25	0.18
Fe_2O_3	0.03	0.01	0.02	0.02	0.02	0.06	0.03	0.02	0.03	0.02
CaO	0.11	0.14	0.10	0.17	0.16	1.82	0.15	0.12	1.22	0.13
Na_2O	10.48	10.33	10.54	9.65	10.47	9.36	10.73	9.87	10.21	10.52
K_2O	0.03	0.04	0.03	0.09	0.08	0.16	0.04	0.03	0.06	0.08
Total	92.22	91.72	92.07	91.66	92.21	96.86	93.29	93.40	92.64	92.43
Si	1.99	2.00	2.01	2.02	2.00	2.13	2.02	2.00	2.03	2.03
Ti	0.00	0.00	0.00	0.00	0.00	0.00	0.00	0.00	0.00	0.00
Al	1.09	1.08	1.06	1.07	1.07	0.88	1.09	1.07	1.07	1.09
Fe^{2+}	0.01	0.00	0.01	0.01	0.00	0.02	0.01	0.01	0.02	0.00
Ca	0.00	0.01	0.00	0.01	0.01	0.07	0.00	0.00	0.02	0.00
Na	0.73	0.72	0.73	0.67	0.73	0.62	0.71	0.69	0.69	0.69
Total	3.83	3.82	3.83	3.78	3.82	3.75	3.84	3.78	3.86	3.83
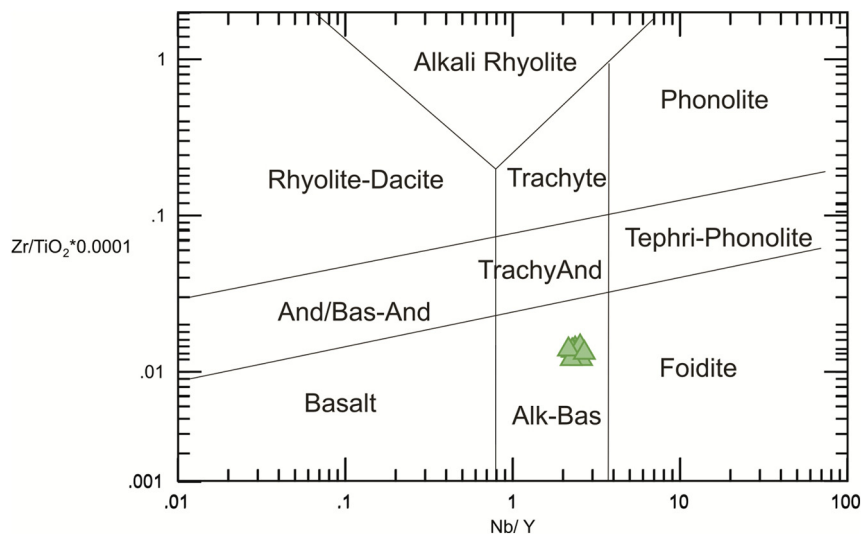
Fig. 8. Classification of TABR according to Winchester and Floyd (1977).

Hart et al. (1989) reported that the basaltic magmas which are influenced by crustal contamination contain La/Nb>1.5 and La/Ta>22. In TABR, the low values of La/Nb (0.50–0.62) and La/Ta (10.52–12.52) ratios, coupled with Sr–Nd isotopic composition (see further on) indicate the magma underwent little or no crustal contamination.

4.3. The role of fractional crystallization and partial melting

According to Kelemen et al. (2004), rocks contain Mg#>60 represent primitive magma composition. All the TABR samples have Mg#>60, represent primitive magma composition.

In TABR, there is no clear correlation among major elements and, Ni, Cr and Co and MgO. The relatively high Mg# (60.28–69.81) and the Ni and Cr content highlight that olivine and clinopyroxene fractionation was not a significant process during magma evolution. In addition, the absence of

plagioclase phenocrysts and the lack of a negative Eu anomaly in TABR reveal that there was no plagioclase fractionation (Fig. 9). Indeed, the high MgO content (10.95–15.49 wt. %) and the lack of correlation between MgO and other oxides support the hypothesis that the fractional crystallization was not a major process in TABR genesis.

The Ti/Al ratios in Cpx composition give constraints about their pressure condition of crystallization (e.g. Wilkinson, 1974; Dobosi et al., 1991; Wlodyka, 2002; Ali and Ntaflos, 2011). The average value of Ti/Al ratio in clinopyroxene cores of TABR is ~0.17, whereas the average value of this ratio in clinopyroxene rims is ~0.22 (Fig. 12). Considering the lower Ti/Al ratio in clinopyroxene cores, they should be crystallized at rather higher pressures than clinopyroxene rims.

The high LREE/HREE ratios indicate low degrees of partial melting (Wilson and Downes, 2006). The differentiation degree of LREE relative to HREE is defined by the $(La/Yb)_N$ ratio, varies from 17.42 to 19.05 with an average of 18.06 in TABR.

Table 4
XRF and ICP analysis of TABR. Major elements, trace and rare earth elements values are given in wt.% and ppm, respectively.

Sample	RD35	RD182	RD85	RD88	RD121	RD121a	RD122	RD123	RD124	RD163	RD72
SiO_2	42.24	43.25	44.66	42.5	43.3	45.21	42.82	42.8	43.12	43.21	43.6
TiO_2	2.35	2.39	2.45	2.41	2.45	2.61	2.47	2.45	2.40	2.48	2.31
Al_2O_2	13.01	13.05	13.27	13.01	13.22	13.42	13.16	13.13	13.26	13.25	13.21
Fe_2O_3	13.28	13.93	13.35	14	13.1	14.3	13.94	14.21	13.91	14.01	13.48
MnO	0.17	0.22	0.27	0.19	0.21	0.25	0.16	0.16	0.21	0.22	0.21
MgO	15.49	13.12	12.1	14.53	14.12	10.95	13.65	13.5	13.45	12.98	13.1
CaO	10.23	10.41	11.29	10.5	10.85	10.2	11.06	11.23	10.88	11.51	11.3
Na_2O	1.73	1.71	2.11	1.87	1.63	2.41	1.75	1.7	1.82	1.98	1.84
K_2O	0.35	0.46	0.49	0.25	0.44	0.39	0.44	0.48	0.39	0.40	0.4
P_2O_5	0.51	0.55	0.54	0.5	0.57	0.48	0.55	0.54	0.49	0.56	0.55
Sum	99.36	99.09	100.5	99.76	99.89	100.22	100	100.2	99.93	100.6	100
L.O.I	2.2	2.1	3.1	3.2	1.5	1.8	2.1	3.2	1.00	1.90	3.08
Ba	1149	997	676	654	1810	1012	660	636	701	759	680
Co	72	61	61	66	60	63	60	61	65	59	64
Cr	358	265	277	299	260	251	270	301	288	301	287
Cu	49	132	49	59	89	94	61	63	40	49	61
Ga	11	18	15	17	14	13	15	15	12	14	12
Hf	3	5	4	4	4	5	4	4	4	3	4
Nb	63	74	70	73	70	73	67	67	69	73	71
Nd	41	36	38	36	36	36	42	42	41	36	40
Ni	289	234	233	260	251	239	231	226	228	242	265
Rb	5	9	9	4	2	4	12	14	11	12	8
Sc	20	26	25	32	29	28	29	28	24	31	27
Sr	589	624	1100	950	1164	1209	887	870	942	641	921
Th	5	6	6	7	6	7	6	6	6	5	6
V	230	275	267	252	241	285	265	271	270	256	267
Y	20.5	21.1	30	26	28	20.4	29	27	27	22.4	25
Zn	62	91	94	98	915	78	97	89	85	91	98
Zr	178	158	198	188	190	175	195	192	200	165	188
La	49.2	46.9				45.8				46.2	
Ce	101	82.0				81.1				83.0	
Pr	10.7	9.27				9.09				9.41	
Sm	6.87	6.79				6.69				6.82	
Eu	2.17	2.17				2.26				2.18	
Gd	6.32	6.18				6.25				6.22	
Tb	0.92	0.95				0.94				0.94	
Dy	4.08	4.31				4.26				4.29	
Ho	0.78	0.82				0.82				0.82	
Er	2.04	2.10				2.11				2.10	
Tm	0.30	0.31				0.31				0.30	
Yb	1.75	1.77				1.79				1.78	
Lu	0.26	0.25				0.26				0.25	
Hf	3.43	3.26				3.55				3.38	
Ta	4.67	3.74				3.84				3.92	
U	2.21	1.59				1.67				1.61	

Sample	RD117	RD118	RD119	RD156
SiO_2	44.25	43.12	42.54	43.09
TiO_2	2.4	2.38	2.4	2.41
Al_2O_2	13.01	13.21	13.11	13.2
Fe_2O_3	13.88	14.01	13.38	13.89
MnO	0.24	0.21	0.18	0.22
MgO	12.86	13.14	14.59	13.05
CaO	10.41	11.09	10.8	10.83
Na_2O	1.9	1.79	2.03	1.95
K_2O	0.47	0.47	0.4	0.45
P_2O_5	0.56	0.58	0.56	0.57
Sum	99.98	100	99.99	99.66
L.O.I	1.89	2.81	1.81	2.25
Ba	797	702	995	712
Co	63	62	69	61
Cr	260	261	331	290

Table 4 (*continued*)

Sample	RD117	RD118	RD119	RD156
Cu	55	58	54	66
Ga	14	14	13	14
Hf	5	4	4	3
Nb	71	68	68	74
Nd	37	43	37	40
Ni	222	228	269	244
Rb	7	5	8	8
Sc	26	28	28	30
Sr	951	912	812	878
Th	6	7	5	5
V	260	252	241	261
Y	25.0	28	23.5	26
Zn	90	92	72	90
Zr	187	185	188	196
La		47.1		
Ce		90		
Pr		9.87		
Sm		6.78		
Eu		2.2		
Gd		6.16		
Tb		0.93		
Dy		4.34		
Ho		0.81		
Er		2.09		
Tm		0.31		
Yb		1.75		
Lu		0.25		
Hf		3.31		
Ta		4.01		
U		1.81		
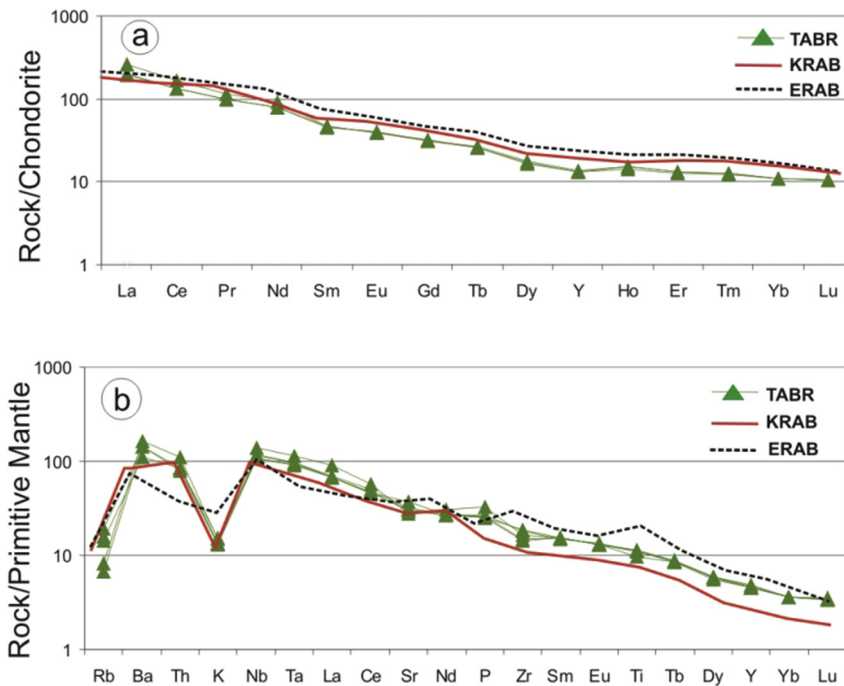
Fig. 9. (a) Chondrite normalized diagram for TABR, Kenya rift alkaline basalts (KRAB) and Ethiopian rift alkaline basalts (ERAB), normalized values are from McDonough and Sun (1995). (b) Primitive mantle normalized diagram for TABR, Kenya rift alkaline basalts (KRAB) and Ethiopian rift alkaline basalts (ERAB), normalized values are from McDonough and Sun (1995).

Table 5
Sm-Nd isotopic analyses of TABR. Initial ($^{143}Nd/^{144}Nd)_0$ ratios and εNd^t_{CHUR} were calculated for a crystallization age of 205Ma. $^{147}Sm/^{144}Nd$ ratios = [(ConcSm/ConcNd)*0.604491]. $^{143}Nd/^{144}Nd$ ratios, normalized to $^{146}Nd/^{144}Nd = 0.7219$ (De Paolo, 1981). εNd (0) corresponds to actual (t = 0) calculated according to the equation = {[($^{143}Nd/^{144}Nd)_{am}/0.512638]-1$]*10^4$, where $^{143}Nd/^{144}Nd_{CHUR} = 0.512638$ (Hamilton et al., 1983). $f_{Sm/Nd} = \{[(^{147}Sm/^{144}Nd)_{am}/0.1967)]-1\}$, where $^{147}Sm/^{144}Nd_{CHUR} = 0.1967$ (Hamilton et al., 1983). Average $^{143}Nd/^{144}Nd$ ratio for the standard JNDi = 0.512100 ± 0.000008. Nd and Sm (in ppm) determined by XRF and ICP, respectively.

Sample	Sm, ppm	Nd, ppm	Sm/Nd	$^{147}Sm/^{144}Nd$	$^{143}Nd/^{144}Nd$	2σ	$(^{143}Nd/^{144}Nd)_0$	εNd_{CHUR}	εNd^t_{CHUR}
RD35	6.87	41.40	0.17	0.1004	0.51269	0.0039	0.51255	1.0	3.5
RD121a	6.69	36.00	0.19	0.1124	0.51277	0.0051	0.51261	2.5	4.7
RD163	6.82	36.50	0.19	0.1130	0.51272	0.0051	0.51256	1.5	3.7
RD182	6.79	36.30	0.19	0.1132	0.51280	0.0049	0.51265	3.1	5.3

Table 6
Rb−Sr isotopic analyses of TABR. Initial ($^{87}Sr/^{86}Sr)_0$ ratios were calculated for a crystallization age of 205 Ma. $^{87}Sr/^{86}Sr$ ratio normalized to the $^{87}Sr/^{86}Sr = 0.1194$. Average $^{87}Sr/^{86}Sr$ ratio for the standard NBS-987 = 0.710244 ± 0.000036. Rb and Sr (in ppm) determined by XRF.

Sample	Rb, ppm	Sr, ppm	Rb/Sr	$^{87}Rb/^{86}Sr$	$^{87}Sr/^{86}Sr$	2σ	$(^{87}Sr/^{86}Sr)_0$
RD35	5.19	589	0.0088	0.0255	0.70522	0.0028	0.70514
RD121a	4.35	1209	0.0036	0.0104	0.70463	0.0037	0.70459
RD163	12.45	641	0.0194	0.0562	0.70493	0.0037	0.70481
RD182	9.21	624	0.0148	0.0427	0.70449	0.0035	0.70432

The high $(La/Yb)_N$, $(Ce/Yb)_N$ (12.00−15.18) and $(Sm/Yb)_N$ (4.07−4.26) ratios suggest a low degree of partial melting in their mantle source (Jung et al., 2006; Wilson and Downes, 2006). The HREE fractionation is represented by the $(Dy/Yb)_N$. The partial melts generated from a garnet-lherzolite

source typically have $(Dy/Yb)_N > 1.06$ (Blundy et al., 1998; Peters et al., 2008). The $(Dy/Yb)_N$ ratio in TABR ranges from 1.52 to 1.62 with an average of 1.57, which implies that the garnet was a residual phase during the partial melting.

For modeling partial melting of common upper mantle sources, REE ratios like the La/Yb vs Dy/Yb (Fig. 13) can be useful (Thirlwall et al., 1994; Baker et al., 1997; Jung et al., 2006). This plot allows to discriminate between melting in the garnet peridotite stability field and spinel peridotite stability field due to the strong fractionation of HREE by garnet. Partial melting in the source magma of TABR was reconstructed (Fig. 13). Partial melting curves were calculated using amodal melting model (Shaw, 1970). Mineralogical composition of primitive mantle (66% olivine, 14% orthopyroxene, 14% clinopyroxene, 6% garnet) and chemical composition of primitive mantle are taken from (Hartmann and Wedepohl, 1990). Mineral-melt distribution coefficients are taken from McKenzie and O'Nions (1991) and normalizing values are from McDonough and Sun (1995). In this diagram samples reveal an origin after about 3%−4% partial melting in the garnet peridotite stability field, generating the primary magma of TABR.
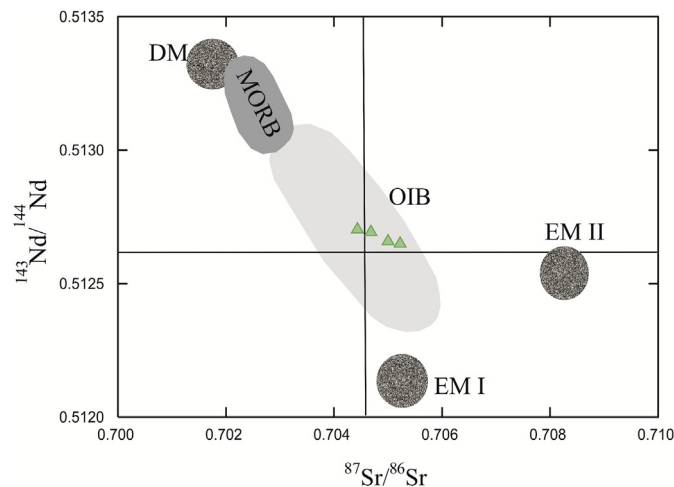

Fig. 10. Sr−Nd isotopic diagram for TABR. Repeated analysis of the NIST − NBS 987 reference standard gave an average of $^{87}Sr/^{87}Sr = 0.71024 ± 0.00004$ (2SD) (n = 45) and no correction was applied for instrumental bias. Repeated measurements of the JNd-i standard (in consistency with La Jolla standard) yielded an average of 143Nd/144Nd of 0.512118 ± 0.000018 (2SD) (n = 45) in agreement within experimental errors with the certified value of 0.5121116. The measured Sr and Nd isotope-ratios were back-calculated to Upper Triassic by using the radioactive decay equation and the proper decay constants (Dickin, 2005). The Sr and Nd isotope ratios were corrected by normalizing to the average $^{87}Sr/^{86}Sr$ ratio for the standard NIST NBS-987 = 0.710244 ± 0.000036 and the average $^{143}Nd/^{144}Nd$ ratio for the standard JNDi = 0.51200 ± 0.000008. The two types enriched mantle (EMI and EMII), depleted MORB mantle (DM) and OIB field are also shown in this diagram.

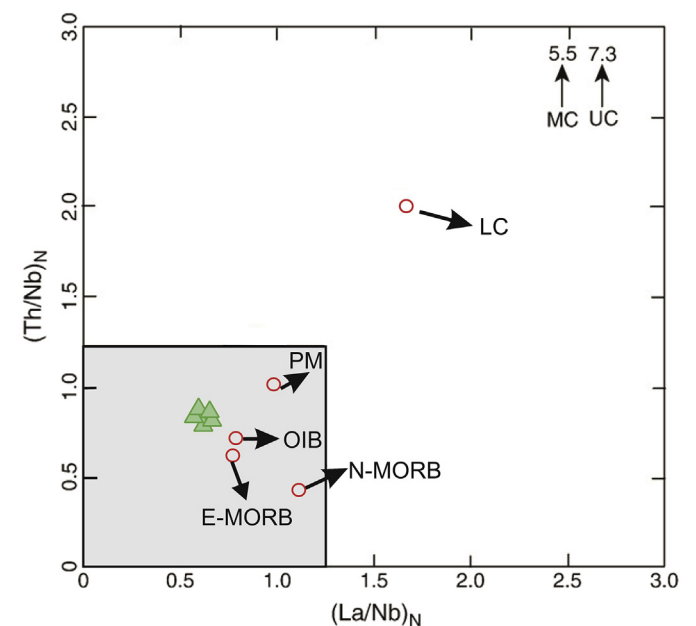Fig. 11. The $(Th/Nb)_N$ vs. $(La/Nb)_N$ diagram for examining the continental crustal contamination of TABR (Dai et al., 2011).
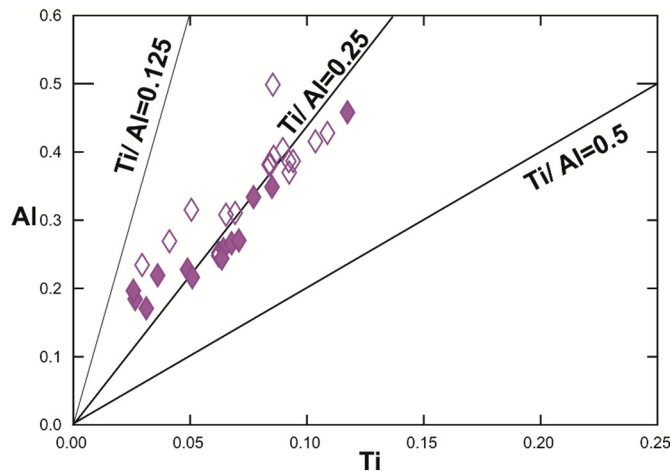
Fig. 12. Ti versus Al diagram in the pyroxenes of TABR. Closed symbols represent phenocryst core whereas open ones represent phenocryst rim.

Some geochemical features like high MgO and low SiO_2 values in alkaline mafic rocks which are formed by partial melting little depend on the source composition, while they more rely on the low degrees of partial melting (~5%) (Hirose and Kushiro, 1993). The relatively high values of MgO (10.95–15.49 wt.%) in TABR could be hence related to the low degrees of partial melting.

4.4. Mantle potential temperature and source characteristics

We used the PRIMELT2.XLS software from Herzberg et al. (2007) to calculate primary magma composition and mantle potential temperature. All rock samples of TABR plot above the dashed-line in Fig. 14 that characterizes olivine-fractionated primary magma from peridotitic sources. For calculating the most proper primary magma composition for TABR, we used the most primitive CA35 sample with Fe_2O_3/TiO_2 = 1.0 to estimate Fe_2O_3 (Herzberg et al., 2007). The calculated primary magma composition was 42.95 SiO_2, 2.36
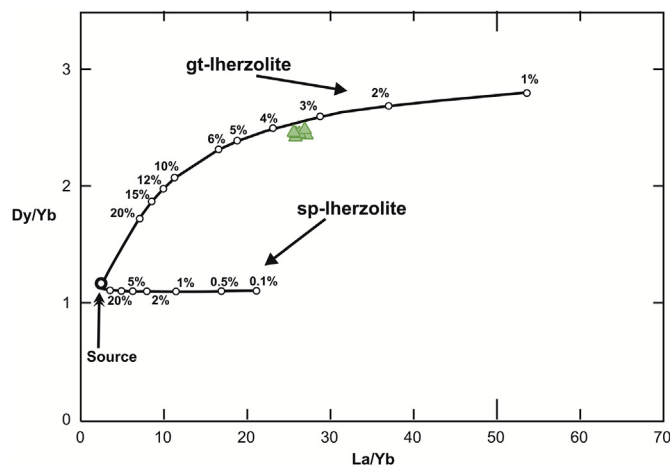

Fig. 13. La/Yb vs Dy/Yb covariation for the TABR. Partial melting curves were calculated using a non-modal, fractional melting model (Shaw, 1970).
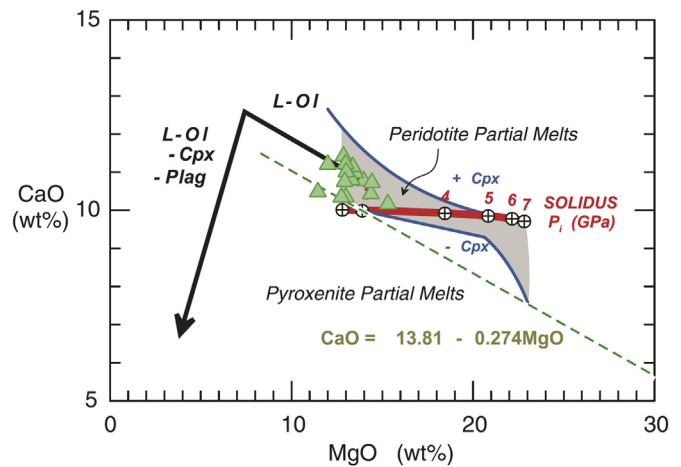

Fig. 14. CaO and MgO diagram of the TABR compared with partial melts of pyroxenite and peridotite (Herzberg et al., 2007).

TiO_2, 13.11 Al_2O_3, 2.36 Fe_2O_3, 10.02 FeO, 16.07 MgO and 10.31 CaO (all in wt.%). The calculated mantle potential temperature for TABR is 1485 °C. The mantle temperature of upper mantle sources beneath MORB is estimated to be about 1454 ± 81 °C (Putirka et al., 2007).

Primitive mantle-normalized multielemental diagrams show patterns resembling typical OIB or intraplate alkaline igneous rocks (Fig. 9b): key features are enrichment of LILE (Ba, Sr and Th), HFSE (Nb, Ta and Zr) and P, and a through at K and HREE (Yb, Lu) which resemble OIBs or intraplate alkaline magmatic rocks (Beccaluva et al., 2002, 2009; Bianchini et al., 2008). For comparison, spider diagrams of Kenya rift alkaline basalts (KRAB) (Späth et al., 2001) and Ethiopian rift alkaline basalts (ERAB) (Beccaluva et al., 2009) are plotted in Fig. 9. The observed patterns of Kenya rift alkaline basalts (KRAB) and Ethiopian rift alkaline basalts (ERAB) in spider diagrams show similarities with TABR. The similarities of REE patterns argue in favor of a rifting basin in Late Triassic. Most of the observations lead to hypothesize that the formation of the TABR occurred in an intraplate tectonic environment. The HFSE/LREE ratio could reveal the source of parental magma. HFSE/LREE ratios less than unity are usually assumed to reflect the derivation from a lithospheric mantle, whereas ratios more than unity are considered to indicate an asthenospheric mantle provenance (Fitton et al., 1991; Smith et al., 1999; Ali et al., 2013). TABR show Nb/La (1.59–1.99), Zr/La (1.81–2.27) and Zr/Ce (1.75–2.15) ratios more than unity which could be interpreted as an origin from an asthenospheric mantle reservoir. Based on rare earth elements and isotopic composition, the study rocks show the similar source characteristics and derivation from the same magmatic source in slightly depleted mantle regard to bulk earth composition (Fig. 15).

4.5. Depth and temperatures of melting

We also used the Visual Basic Excel Macro thermobarometer of Lee et al. (2009) that is based on SiO_2 and MgO
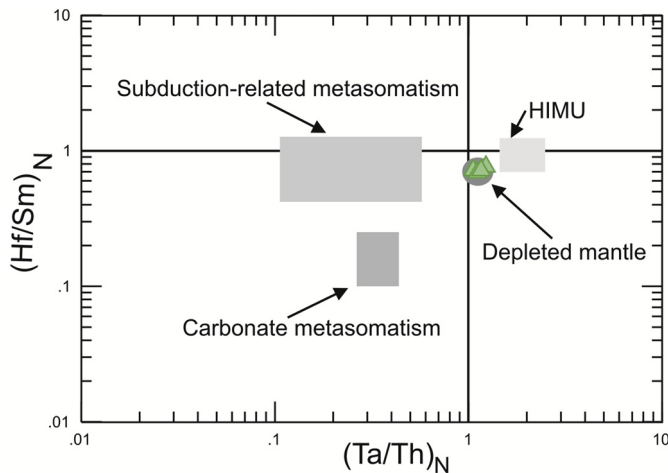
Fig. 15. TABR samples in the diagram of (Ta/Th)$_N$ and (Hf/Sm)$_N$ from Wang et al. (2006). All samples locate in the field of depleted mantle.

contents of mafic magma to constrain the pressures and temperatures of magma generation. According to the thermobarometer of Lee et al. (2009), the primitive samples of TABR which contain 10.95 wt.%<MgO<15.49 wt.%, could have been generated at pressures 2.1–3.2 GPa (corresponding to a depth of about 66–101 km). Also based on the Albarède (1992) barometer, TABR could form at pressures of 2.2–3.6 GPa (corresponding to a depth of about 72–114 km). The calculated melting temperatures of the TABR vary from 1420 °C to 1510 °C (Lee et al., 2009) or from 1380 °C to 1450 °C (Putirka, 2005). The calculated depth and temperature of magma generation imply that the melting could have been occurred within the asthenospheric mantle in the garnet stability field.

Alborz zone reveals an elevation 3000–5000 m above sea level. According to geophysical studies, mantle lithosphere is almost absent underneath the Alborz Mountains (e.g., Sodoudi et al., 2009; Mirnejad et al., 2010). The crustal thickness under the central Alborz is estimated to be about 35–45 km (Dehghani and Makris, 1984; Amjadi et al., 2012). However inadequate crustal base and the relatively thin lithosphere underneath the Alborz can indicate that the asthenospheric mantle is supporting the high elevation (Sodoudi et al., 2009). Based on the thermobarometry calculations, the magma segregation depth of TABR which is about 66–101 km (Lee et al., 2009) or 72–114 km (Albarède, 1992) defines the location of their magma source region in the asthenospheric mantle. Also the calculated mantle potential temperature is consistent with the hypothesis that TABR formed from the mantle at an ambient temperature which rules out the mantle plume hypothesis (Hastie and Kerr, 2010). It is hence proposed that TABR were formed by the extension and partial melting of asthenospheric mantle in the late Triassic (Rhaetic rift basin) without major contribution of subcontinental lithospheric mantle or crustal contamination.

5. Conclusion

The geochemical features of TABR indicate that they are close to a primary magma compositions and that fractional crystallization was not a major process during their evolution. The low ratios of Zr/Nb, La/Nb and La/Ta along with the lack of Ti negative anomaly in mantle-normalized multilemental diagrams preclude any significant crustal contamination or interaction with lithospheric mantle in their genesis.

It is proposed that the source magma of TABR was generated by the low degree of partial melting from a garnet-bearing mantle source. Based on $^{87}Sr/^{86}Sr$, $^{143}Nd/^{144}Nd$ and HFSE/REE ratios TABR should derived from the slightly depleted mantle source with respect to bulk Earth composition.

The depth of magma generation of these rocks is hypothesized at about 66–114 km. The melting temperatures calculated for TABR vary from approximately from 1380 °C to 1510 °C. The calculated mantle source temperature argues against the mantle plume hypothesis in the genesis of TABR.

It can be conclude that TABR were produced by the up-welling and decompressional melting of an asthenospheric mantle in the rifting basin in Late Triassic, without major involvement of subcontinental lithospheric mantle or crustal contamination.

References

Adamia, S.A., Lordkipanidmze, M.B., Zakariadze, G.S., 1977. Evolution of an active continental margin as exemplified by the Alpine history of the Caucasus. Tectonophysics 40, 183–199.

Alavi, M., 1996. Tectonostratigraphic synthesis and structural style of the Alborz mountain system in Northern Iran. J. Geodyn. 21, 1–33.

Albarède, F., 1992. How deep do common basaltic magmas form and differentiate? J. Geophys. Res. 97, 10997–11009.

Allenbach, P., 1966. Geology and petrography of Damavand and its surroundings (Central Alborz), 63. Geological institute, ETH-Zurich, Mitteilung, Iran, pp. 1–114.

Ali, S., Ntaflos, T., 2011. Alkali basalts from Burgenland, Austria: petrological constraints on the origin of the westernmost magmatism in the Carpathian–Pannonian region. Lithos 121, 176–188.

Ali, S., Ntaflos, T., Upton, B.J.G., 2013. Petrogenesis and mantle source characteristics of Quaternary alkaline mafic lavas in the western Carpathian–Pannonian Region, Styria, Austria. Chem. Geol. 337–338, 99–114.

Amjadi, A., Moteshrei, A., Theroied, S.A.A., Ansari, M.R., 2012. Estimation of Moho depth using Bouguer anomaly gravity data. Innova Ciencia l4, 7–14.

Assereto, R., 1966. Geological Map of Upper Diajrud and Lar Valleys (Central Elborz, Iran), pp. Publ.N. 86, 232. Inst. Geol. Univ. Milano, Italy.

Annels, R.N., Arturton, R.S., Bazley, R.A.B., Davis, R.C., Hamedi, M., Rahimzahed, F., Rashtian, K., 1985. Explanatory Text of the Qazvin and Rasht Quadrangle Map. Geological Survey of Iran, Tehran, Iran, 94 pp.

Baker, J.A., Menzies, M.A., Thirlwall, M.F., Macpherson, C.G., 1997. Petrogenesis of quaternary intraplate volcanism, Sana'a, Yemen: implications for plume–lithosphere interaction and polybaric melt hybridization. J. Petrol. 38, 1359–1390.

Bardintzeff, J., Deniel, C., Guillou, H., Platevoet, B., Telouk, P.M., Oun, K.h., 2012. Miocene to recent alkaline volcanism between Al Haruj and Waw an

Namous (southern Libya). Int. J. Earth Sci. (Geol. Rundsch.) 101, 1047—1063.

Beccaluva, L., Coltorti, M., Di Girolamo, P., Melluso, L., Milani, L., Morra, V., Siena, F., 2002. Petrogenesis and evolution of Mt. Vulture alkaline volcanism (Southern Italy). Mineral. Petrol. 74, 277—297.

Beccaluva, L., Bianchini, G., Natali, C., Siena, F., 2009. Continental flood basalts and mantle plumes: a case study of the Northern Ethiopian Plateau. J. Petrol. 50, 1377—1403.

Berberian, M., 1983. The southern Caspian: a compressional depression floored by a trapped, modified oceanic crust. Can. J. Earth Sci. 20, 163—183.

Berberian, M., King, G.C.P., 1981. Towards a paleogeography and tectonic evolution of Iran. Can. J. Earth Sci. 18, 210—265.

Berberian, F., Muir, I.D., Pankhurst, R.J., Berberian, M., 1982. Late Creta- ceous and Early Miocene Andean-type plutonic activity in northern Makran and Central Iran. J. Geol. Soc. Lond. 139, 605—614.

Best, M.G., 2002. Igneous and Metamorphic Petrology. Blackwell Publishing. ISBN 1-4051-0588-7.

Bianchini, G., Beccaluva, L., Siena, F., 2008. Post-collisional and intraplate Cenozoic volcanism in the rifted Apennines/Adriatic domain. Lithos 101, 125—140.

Bienvenu, P., Bougault, H., Joron, J., Treuil, M., Dmitriev, L., 1990. MORB alteration: rareearthelement/non-rare-earth hygromagmaphile element fractionation. Chem. Geol. 82, 1—14.

Blundy, J.D., Robinson, J.A.C., Wood, B.J., 1998. Heavy REE are compatible in clinopyroxene on the spinel lherzolite solidus. Earth Planet Sci. Lett. 160, 493—504.

Brunet, M.F., Korateav, M.W., Arshov, A.V., Nikishin, A.M., 2003. The south Caspian Basin: a review of its evolution from subsidence modeling. Sediment. Geol. 148, 119—156.

Cartier, E.G., 1971. Die Geologic des unteren Chalus Tals, Zentral-Alborz, Iran. Inaugural-Dissertation zur Erlangtmg der Philosophischen Dok- torwiirde, vorgelegt der Philosophischen Fakult/it II, der Universit~it Z/Jrich.

Dai, J., Wang, C., Hébert, R., Li, Y., Zhong, H., Guillaume, R., Bezard, B., Wei, Y., 2011. Late Devonian OIB alkaline gabbro in the Yarlung Zangbo suture zone: remnants of the Paleo-tethys? Gondwana Res. 19, 232—243.

Deer, A., Howie, R., Wise, W.S., Zussman, J., 2004. Rock Forming Minerals. Vol. 4B. Framework Silicates: Silica Minerals, Feldspathoids and the Ze- olites. The Geological Society, London, pp. 546—560.

Dehghani, G., Makris, J., 1984. The gravity field and crustal structure of Iran. Neues Jahrbuch Geol. Palaontol. Abhand. 168, 215—229.

Dobosi, G., Schultz-Güttler, R., Kurat, G., Kracher, A., 1991. Pyroxene chemistry and evolution of alkali basaltic rocks from Burgenland and Styria, Austria. Mineral. Petrol. 43, 275—292.

De Paolo, D.J., 1981. Neodymium isotopes in the Colorado front range and implications for crust formation and mantle evolution in the Proterozoic. Nature 291, 193—197.

Dickin, A.P., 2005. Radiogenic Isotope Geology. Cambridge University Press, 492 pp.

Fauvelet, F., Eftekhar Nezhad, J., 1992. Explanatory Text of the Gonbad Quadrangle Map (1/250000). Geological Survey of Iran, Tehran.

Fitton, J.G., James, D., Leeman, W.P., 1991. Basic magmatism associated with Late Cenozoic extension in the Western United States: compositional variations in space and time. J. Geophys. Res. 96, 13693—13711.

Franzini, M., Leoni, L., Saitta, M., 1975. Revisione di una metodologia ana- litica fluorescenza-X basata sulla correzione completa degli effetti di matrice. Rend. Soc. Ital. Miner. Petrol 31, 365—378.

Gupta, A.K., Fyfe, W.S., 1975. Leucite survival: the alteration to analcime. Can. Mineral. 13, 361—363.

Hallman, A., 1996. Gondwana and Tethys, vol. 37. Geological Society [London] Special Publication, pp. 119—181.

Hamilton, P.J., O'Nions, R.K., Bridgwater, D., Nutman, A., 1983. Sm-Nd studies of Archaean metasediments and metavolcanics from West Greenland and their implications for the Earth's early history. Earth Planet. Sci. Lett. 62, 263—272.

Hart, W.K., Wolde, G.C., Walter, R.C., Mertzman, S.A., 1989. Basaltic volcanism in Ethiopia: constraints on continental rifting and mantle in- teractions. J. Geophys. Res. 94, 7731—7748.

Hartmann, G., Wedepohl, K.H., 1990. Metasomatically altered peridotite xe- noliths from the hessian depression (Northwest Germany). Geochem. Cosmochim. Acta 54, 71—86.

Hastie, A.R., Kerr, A.C., 2010. Mantle plume or slab window? Physical and geochemical constraints on the origin of the Caribbean oceanic plateau. Earth Sci. Rev. 98, 283—293.

Hawkesworth, C.J., Vollmer, R., 1979. Crustal contamination versus enriched mantle: 143Nd/144Nd and 87Sr/86Sr evidence from the Italian volcanics. Contrib. Mineral. Petrol. 69, 151—165.

Herzberg, C., Asimow, P.D., Arndt, N., Niu, Y., Lesher, C.M., Fitton, J.G., Cheadle, M.J., Saunders, A.D., 2007. Temperatures in ambient mantle and plumes: constraints from basalts, picrites, and komatiites. Geochem. Geophys. Geosyst. 8 https://doi.org/10.1029/2006GC001390.

Hirose, K., Kushiro, I., 1993. Partial melting of dry peridotites at high pressures: determination of compositions of melts segregated from peri- dotite using aggregates of diamond. Earth Planet Sci. Lett. 114, 4477—4489.

Jung, C., 2003. Geochemische und isotopen geochemische Untersuchungen an tertiaeren Vulkantien der Hocheifel-ein beitrag zur identizierung der mantelquellen von Rift bezogenen Vulkaniten. Dissertation zur Erlangung des doktorgardes Naturwissenchaftin, vorgelegt dem fachbreich Geo- wissenschaftin der Philipps Universitaet Marburg.

Jung, C., Jung, S., Hoffer, E., Berndt, J., 2006. Petrogenesis of Tertiary Mafic alkaline magmas in the Hocheifel,Germany. J. Petrol. 47, 1637—1671.

Kelemen, P.B., Hanghoj, K., Green, A.R., 2004. One view of the geochemistry of subduction-related magmatic arcs. With an emphasis on primitive Andesite and lower crust. Treatise Geochem. 3, 593—659.

Lee, C.-T., Luffi, P., Plank, T., Dalton, H., Leeman, W.P., 2009. Constraints on the depths and temperatures of basaltic magma generation on earth and other terrestrial planets using new thermobarometers for mafic magmas. Earth Planet. Sci. Lett. 279, 20—33.

Leoni, L., Saitta, M., 1976. X-ray fluorescence analysis of 29 trace elements in rocks and mineral standards. Rend. Soc. Ital. Miner. Petrol 32, 497—510.

Luhr, J.F., Kyser, T.K., 1989. Primary Igneous Analcime: the Colima Amer- ican Mineralogist, vol. 74, pp. 216—223.

McBirney, A.R., 2006. Igneous Petrology, third ed. Jones and Bartlett, Sud- bury, MA. 550 pp.

McDonough, W.F., Sun, S.S., 1995. Composition of the earth. Chem. Geol. 120, 223—253.

McKenzie, D.P., Bickle, M.J., 1988. The volume and composition of melt generated by extension of the lithospheric. J. Petrol. 29, 625—679.

McKenzie, D., O'Nions, R.K., 1991. Partial melt distributions from inversion of rare earth element concentrations. J. Petrol. 32, 1021—1091.

Mirnejad, H., Hassanzadeh, J., Cousens, B.L., Taylor, B.E., 2010. Geochem- ical evidence for deep mantle melting and lithospheric delamination as the origin of the inland Damavand volcanic rocks of northern Iran. J. Volcanol. Geoth. Res. 198, 288—296.

Morata, D., Higueras, P., 1996. Analcimas en lavas alcalinas delSinclinal de Almadén, Origen primario o secundario? Implicaciones petrogenéticas. Boletín de la Sociedad Espanõla de Mineralogía 19, 27—37.

Morata, D., Aguirre, L., Féraud, G., Belmar, M., 2005. In: 6th International Symposium on Andean Geodynamics, pp. 531—534. Barcelona.

Morimoto, N., Fabries, J., Fergusson, A.K., Guizbourg, I.D., Ross, M., Seifert, F.A., Zussman, J., Aoki, K., Gottardi, G., 1988. Nomenclature of pyroxenes. Am. Mineral. 173, 1123—1133.

Nabavi, M.H., Seyed Emami, K., 1977. Sinrmurian ammonites from the Shemshak Formation of the north Iran (Semnan area. Alborz). N. Jb.Geol.Palaont. Abhand 153, 70—85.

Nazari, H., 2006. Analyse de la tectonique recente et active dans l Alborz Central et la region de Tehreran: Approche morphotectonique et paleo- seismologique. theses PhD. Montpellier ll, Montpellier, France, p. 110.

Nazari, H., Omrani, J., Shahidi, A.R., 2004. Geological Map of Anzali, Scale 1:100000. Geological Survey of Iran.

Nazari, H., Shahidi, A., 2011. Tectonic of Iran « Alborz ». Gological Survey and Mineral Exploration of Iran, Research institute for Earth Science, 97 pp.

Pearce, J., Cann, J., 1973. Tectonic setting of basic volcanic rocks determined using trace element analyses. Earth Planet. Sci. Lett. 19, 290—300.

Peters, T.J., Menzies, M., Thitlwall, M., Kyle, P.K., 2008. Zuni-Bandera volcanism, Rio Grande, USA, Melt formation in garnet-and spinel −facies mantle straddling the asthenosphere −lithosphere boundary. Lithos 102, 295−315.

Pouchou, J.L., Pichoir, F., 1984. Un nouveau modèle de calcul pour la microanalise quantitative par spectrométrie de rayon-X: I. Application à l'analyse d'échantillons homogènes. La Recherche Aérospatiale 3, 167−192.

Putirka, K.D., 2005. Mantle potential temperatures at Hawaii, Iceland, and the mid- oceanridge system, as inferred from olivine phenocrysts: evidence for thermally driven mantle plumes. Geochem. Geophys. Geosyst. 6 https://doi.org/10.1029/2005GC000915.

Putirka, K.D., Perfit, M., Ryerson, F.J., Jackson, M.G., 2007. Ambient and excess mantle temperatures, olivine thermometry, and active vs. passive upwelling. Chem. Geol. 177−206.

Rollinson, H., 1993. Using Geochemical Data: Evaluation, Presentation, Interpretation. Longman Scientific and Technical, 352 pp.

Sabzehei, M., 1993. Calendrier de la migration permo-triasique et morcellement mésozoique des éléments continentauz de l Iran, These. Univ. Pierre et Marie Curie, Paris, France, 298 pp.

Saidi, A., Ghassemi, M.R., 1993. Geological Map of 1/100000 Baladeh. Geological Survey of Iran, Iran.

Seyed Emami, K., 2003. Triassic in Iran. Facies 48, 91−196.

Shahidi, A., 2005. Evolution tectonique et géodynamique des chaines de l Alborz et du Kopet-Dagh (Iran) depuise le Mésozoique. Journées des Doctorants, 3 et 4 mai, Ecole des Mines de Paris.

Shahidi, A., 2008. Evolution tectonique du Nord de L Iran (Alborz et Kopet-Dagh) depuis le Mésozoique. PhD Thése. Université Pierre et Marie Curie, Paris, 500 pp.

Shaw, D.M., 1970. Trace element fractionation during anatexis. Geochem. Cosmochim. Acta 34, 237−243.

Stampfli, G.M., 1978. Etude Géologique générale del'Elburz oriental au S de Gonbad-e-Qabus Iran N-E. PhD Thesis, Genève, 315 pp.

Stampfli, G.M., Marcoux, J., Baud, A., 1991. Tethyan margins in space and time. Palaeogeogr. Palaeoclimatol. Palaeoecol. 87, 373−409.

Steiger, R., 1966. Die geologie der west-Firuzkuh area (Zentralelburz/Iran). Mitteilungen aus dem Geologischen Institut der Eidgen6ssischen Technischen Hochschule und der Universitiit Zurich, 145 pp.

Stocklin, J., 1974. Northern Iran: Alborz Mountains. In: Spencer, A.M. (Ed.), Mesozoic−cenozoic Orogenic Belts; Data for Orogenic Studies; Alpine-Himalayan Orogens, vol. 4. Geological Society [London] Special Publication, pp. 213−234.

Sodoudi, F., Yuan, X., Kind, R., Heit, B., Sadidkhouy, A., 2009. Evidence for a missing crustal root and a thin lithosphere beneath the Central Alborz by receiver function studies. Geophys. J. Int. 177, 733−742.

Smith, E.I., Sánchez, A., Walker, J.D., Wang, K., 1999. Geochemistry of mafic magmas in the Hurricane Volcanic Field, Utah: implications for small- and large scale chemical variability of the lithospheric mantle. J. Geol. 107433−107448.

Späth, A., Le Roex, A.P., Opiyo-Akech, N., 2001. Plume−lithosphere interaction and the origin of continental rift-related alkaline volcanism—the Chyulu Hills Volcanic Province, southern Kenya. J. Petrol. 42, 765−787.

Taylor, D., Mackenzie, W.S., 1975. A contribution to the pseudoleucite problem. Contrib. Mineral. Petrol. 49, 321−333.

Thirlwall, M.F., Smith, T.E., Graham, A.M., Theodorou, N., Hollings, P., Davidson, J.P., Arculus, R.J., 1994. High field strength element anomalies in arc lavas: source or process? J. Petrol. 35, 819−838.

Vahdati Daneshmand, F., Nadim, H., 1999. Geological Map of Marzanabad Quadrangle. Geological Survey of Iran.

Wang, Y.J., Fan, W.M., Zhang, H.F., Peng, T.P., 2006. Early Cretaceous gabbroic rocks from the Taihang Mountains: implications for a paleo-subduction- related lithospheric mantle beneath the central North China Craton. Lithos 86, 281−302.

Weaver, B.L., 1991. The origin of ocean island basalt end member compositions: trace elements and isotopic constrains. Earth Planet Sci. Lett. 104, 3810−3897.

Wilson, M., 1989. Igneouse Petrogenesis a Global Tectonical Approach. originally published by Chapman and Hall, 466 pp.

Wilson, M., Downes, H., 2006. Tertiary−Quaternary intra-plate magmatism in Europe and its relation to mantle dynamics. In: Gee, D.G., Stephenson, R.A. (Eds.), European Lithosphere DynamicsGeological Society of London, Memoirs, vol. 32, pp. 147−166.

Winchester, J.A., Floyd, P.A., 1977. Geochemical discrimination of different magma series and their differentiation products using immobile elements. Chem. Geol. 20, 325−343.

Wlodyka, R., 2002. Clinopyroxene and amphibole zoning patterns in teschnite rocks from the outer western polish carpatians. In: Congress of Carpatian-Balkan Geological Association Bratislava, September 1st-4th.

Wörner, G., 1999. Lithospheric dynamics and mantle sources of alkaline magmatism of the Cenozoic west Antarctic rift system. Global Planet. Change 23, 61−77.

Wilkinson, J.F.G., 1974. Garnet clinopyroxenite inclusions from diatremes in the Gloucester area, New South Wales. Contrib. Mineral. Petrol. 46, 275−299.